AAS 25-161

NUMERICAL ASSESSMENT OF INTERMEDIATE MODELS IN A FREQUENCY-BASED HIERARCHY FOR THE CISLUNAR DOMAIN

Beom Park*, Rohith Reddy Sanaga*, Kathleen C. Howell†

A frequency-based hierarchy of dynamical models in cislunar space is introduced in recent literature, where multiple models between the Circular Restricted Three-Body Problem (CR3BP) and a Higher-Fidelity Ephemeris Model (HFEM) are investigated within a common rotating reference frame. The primary objective of the current investigation is a focus on extensive numerical examples across cislunar space to complement and further develop the hierarchy. Employing various numerical methods, the evolution of CR3BP structures within the HFEM and intermediate models is examined. The capabilities of various intermediate models in bridging the gap between the CR3BP and HFEM are analyzed within the frequency domain.

INTRODUCTION

When addressing astrodynamics problems, understanding the hierarchy of various dynamical models aids in selecting a suitable model for specific analyses. Within cislunar space, such a hierarchy remains somewhat elusive due to the complex gravitational environment originating from the influence of both Earth and Moon. While the Earth-Moon Circular Restricted Three-Body Problem (CR3BP) undoubtedly serves as an invaluable lower-fidelity model in the cislunar dynamical regime, identifying suitable intermediate models to bridge the gap between the CR3BP and a higher-fidelity model remains an open question.

One key aspect in investigating the model hierarchy is to understand the multiple dynamical factors that alter the desired path between the CR3BP and a higher-fidelity model altogether. Previous endeavors to characterize these factors in cislunar space are generally categorized into three different approaches* as illustrated in Fig. 1, and detailed as follows:

(Approach 1) Top-down: In this strategy, a Higher-Fidelity Ephemeris Model (HFEM) is characterized *first* to provide understanding for the components that are not modeled within the Earth-Moon CR3BP. Gómez, Masdemont, and Mondelo [1] supply the theoretical foundation for this strategy, where a Sun-Earth-Moon point-mass HFEM is approximated as a dynamical model that includes quasi-periodic perturbations governed by five distinct frequencies within a common reference frame. Such a formulation is adapted in Park and Howell [2], where a change in independent variables is suggested to isolate the time-autonomous CR3BP dynamics and extract the perturbations that exist *in addition to* the CR3BP. Then, it is possible to envision a *frequency*-based model hierarchy within cislunar space as illustrated in Fig. 1 where the fidelity of the dynamical models is generally increased via introducing perturbations associated with distinct frequencies [1, 3]. Leveraging this concept, the capabilities and limitations of intermediate models that typically introduce one or two perturbing frequencies are *globally* characterized [2,3], providing a theoretical foundation for understanding the model hierarchy within the cislunar regime.

(Approach 2) Bottom-up: In this strategy, sample CR3BP structures are evolved within intermediate models to gauge the influence of the selectively introduced perturbations. Numerous authors address this approach [4–9]. These various investigations may be classified in terms of (i) the intermediate model under investigation,

*Ph.D. Candidate, School of Aeronautics and Astronautics, Purdue University, West Lafayette, IN 47907
†Hsu Lo Distinguished Professor, School of Aeronautics and Astronautics, Purdue University, West Lafayette, IN 47907

*While the current analysis focuses on the Earth-Moon system, these various approaches are also applicable for investigating model hierarchies in other systems, e.g., the Sun-Earth system.

(ii) the employed numerical scheme that often takes either semi-analytical or fully numerical forms, and (iii) the sample CR3BP structures. This bottom-up approach is relatively local, focusing on specific regions of interest within cislunar space. However, it provides a valuable complementary perspective to the top-down approach, offering concrete numerical experiments for the evolution of the CR3BP structures under selected perturbations in ideal forms.

(Approach 3) Direct transition from the CR3BP to the HFEM: In this approach, the intermediate models are not explicitly incorporated. Rather, a numerical scheme, typically a differential corrector, is employed to directly locate HFEM analogs originating from an initial guess provided by the CR3BP solutions. For instance, the HFEM counterparts for the CR3BP Lagrange points as well as periodic orbits are previously discussed [10–14]. The specific numerical scheme for the transition process itself is also a topic for investigation; different numerical transition schemes are analyzed [10–15] to construct HFEM analogs.

Note that these three different approaches are not always mutually exclusive, where multiple strategies may be combined to yield a more complete analysis. For example, the theoretical, top-down approach is complemented by numerical transition examples [1–3]. Multiple authors suggest leveraging the structures from the intermediate models as a type of evolving initial guess for the HFEM analogs [16–18]. Such a strategy may be considered a combination of the bottom-up and direct transition approaches. While the categorization of these three approaches provides useful insights on the state of the art and highlights potential knowledge gaps regarding the model hierarchy within cislunar space, integration of different strategies usually aids in a more comprehensive understanding.

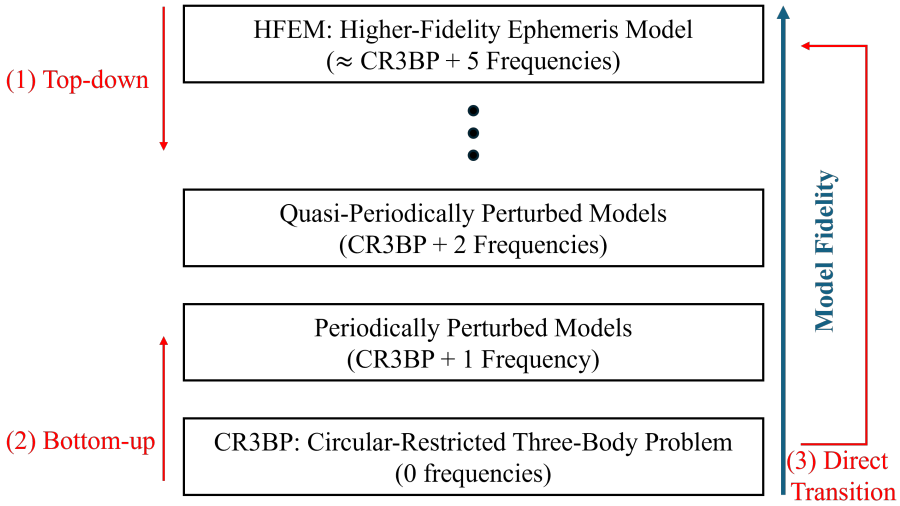

Fig. 1: Frequency-based model hierarchy and three approaches (adapted from Park, Sanaga, and Howell [3])

The main objective of the current investigation is to further elucidate the frequency-based model hierarchy within the cislunar environment. The objective entails a holistic process that combines all three approaches as discussed previously, while focusing on expanding the numerical examples for the evolution of the CR3BP structures in various intermediate models as well as HFEM. More specifically, the following goals are noted along the related knowledge gaps:

(Goal 1) Investigate the evolution of multiple CR3BP structures in terms of solution geometry within various dynamical models along the hierarchy: the geometry change in CR3BP structures for different models is recorded leveraging a common rotating reference frame. The analysis attempts to provide numerical experiments to clarify the model hierarchy. To that end, various structures including the Lagrange points and multiple periodic orbits in the lunar vicinity are investigated. Rather than focusing on one or a few intermediate models, multiple models within the model hierarchy are considered simultaneously, providing a more thorough analysis. While numerous options for the intermediate models potentially exist, the ones that are characterized by Park and Howell [2] as well as Park, Sanaga, and Howell [3] are examined. These

models include four different periodically perturbed models as well as two quasi-periodically perturbed models. Then, the counterparts within these various models are supplied via various numerical methods, leveraging the underlying Hamiltonian structures. The behaviors across different intermediate models are juxtaposed to gauge the relative importance of additional components along the model hierarchy.

(Goal 2) Concretely compare the analogs within the HFEM and the corresponding structures within intermediate models: Numerical investigation of the counterparts within the intermediate models and the HFEM leverages the (Approach 2) bottom-up and (Approach 3) direct transition, respectively. In previous literature, typically, only one of two approaches is examined, supplying incomplete insights on the model hierarchy. Relatively few sources [2, 8, 14, 19] attempt to combine these two strategies and concretely demonstrate that the information available within the intermediate model indeed persists in the HFEM. These previous works offer local analysis that focuses on specific regions, e.g., the vicinity of L_4, as well as leverages a single intermediate model, e.g., the BCR4BP. In the current investigation, these efforts are extended to various structures across cislunar space and employing multiple intermediate models. The geometry evolution in the HFEM and the intermediate models is compared via Fourier analysis. The investigation reveals that the HFEM structures leverage the Hamiltonian structures constructed within the intermediate models. Then, the relative amplitudes associated with structures emerging as a result of different frequencies clarify the most dominant perturbing frequency specific to different regions within cislunar space.

The insights as a consequence of this investigation serve as criteria to select dynamical models suited for various theoretical and practical astrodynamics problems within the cislunar domain.

Any model hierarchy is a nuanced concept within the cislunar environment and the current investigation introduces several assumptions to aid in clear analysis. First, the HFEM includes the point-mass gravity from the Sun-Earth-Moon system described by the JPL ephemerides DE440 [20]; additional perturbations, e.g., solar radiation pressure, are not considered. Also, due to numerical and dynamical issues, some CR3BP structures do not allow well-defined HFEM counterparts [8, 14]. Such CR3BP structures are omitted from the current analysis and remain within the scope of future investigations. While the evolution of the CR3BP solution geometry is currently investigated, different aspects may be relevant in characterizing the "fidelity." For example, the evolution of the stability associated with the CR3BP solutions or the line-of-sight information for specific targets may alter the model hierarchy that is discussed within the current investigation. Lastly, the current analysis focuses on the *description* of the model hierarchy itself; it does not suggest that incorporating intermediate models is necessarily *better* as opposed to directly transitioning from the CR3BP to the HFEM.

The rest of the document is organized as follows. The equations of motion for the intermediate models and the HFEM are initially reviewed. Then, the numerical schemes to supply and analyze counterparts within multiple dynamical models are summarized. Subsequently, the evolution of the CR3BP Lagrange points in different dynamical models is discussed, followed by an investigation of the evolution of CR3BP periodic orbits in the lunar vicinity. Finally, concluding remarks are provided.

DYNAMICAL MODELS

Common Reference Frame and Independent Variable

Pulsating-Rotating Reference Frame Multiple dynamical models under investigation are represented in a common rotating reference frame, also denoted as the pulsating-rotating frame, described by the orthogonal unit vectors $\hat{x} - \hat{y} - \hat{z}$. The origin of the frame is the Earth-Moon barycenter (B). The unit vector, $\hat{x}$, is directed from the Earth to the Moon. The direction of the angular momentum vector for the Moon with respect to the Earth coincides with $\hat{z}$, and the $\hat{y}$-axis completes the dextral triad. Depending on the model, these vectors are instantaneously determined, e.g., the angular momentum vector direction is not constant within the HFEM. The frame adopts a nondimensional (nd) representation of length, where the Earth-Moon distance appears as a unit length regardless of its instantaneous dimensional distance. Then, the locations of the Earth and the Moon are fixed within the frame on the $\hat{x}$-axis at $-\mu$ and $1 - \mu$, respectively, where μ is the mass ratio of the Moon with respect to the Earth-Moon system. More discussions on the relationship between this pulsating-rotating frame to other commonly adopted frames are provided in Park, Sanaga, and Howell [3].

Independent Variable: Pulsating Nondimensional Time As different dynamical models are typically derived independently from each other, there exists some arbitrariness in relating the independent (time) variables from multiple models. Consider the dimensional time, T, and two nd time variables, t_*, t, defined through the following rate of change with respect to T,

$$\frac{dt_*}{dT} = t'_* = \sqrt{\frac{\mu_*}{l_*^3}}, \quad \frac{dt}{dT} = t' = \sqrt{\frac{\mu_*}{l^3}}. \tag{1}$$

The gravitational parameter for the Earth-Moon system is μ_*, and l_* is an arbitrary Earth-Moon characteristic length that is constant; one possible definition for l_* is an average of the Earth-Moon distance obtained from the ephemerides. Thus, t_* evolves at a constant rate with respect to the dimensional time. The Earth-Moon distance that varies as described differently in each dynamical model is denoted as l without the asterisk. Then, t is defined such that the rate of the change with respect to T depends on the instantaneous Earth-Moon distance, l. These two nd time variables are denoted as uniform and non-uniform (or, pulsating) times. Park and Howell [2] demonstrate that the pulsating time is more resilient to the varying Earth-Moon distance and results in better velocity scaling properties between different models in the lunar vicinity. It is better suited for comparing the isochronous results from different dynamical models, e.g., Fourier analysis [21]. Thus, the common independent variable for the current investigation adopts t, i.e., non-uniform time, rather than T, t_*.

Dynamical Models within the Common Formulation

The different dynamical models that are under investigation are briefly reviewed. All models share two common assumptions: (i) celestial bodies are approximated as point-masses, and (ii) the spacecraft does not influence the motion of the celestial bodies (the "restricted" property). The CR3BP represents the simplest representation for behavior in the Earth-Moon system, assuming its mutual motion to be circular. The Higher-Fidelity Ephemeris Model (HFEM) in the current analysis introduces the Earth-Moon-Sun as the gravitational bodies, whose locations are retrieved from the ephemerides. Then, the intermediate models add varying levels of complexity to bridge the gap between the CR3BP and HFEM. These models are detailed in Table 1 along with key "fidelity" characteristics; more check marks (✓) imply additional components that are introduced within the intermediate models. The first four models in the table represent periodic extensions of the CR3BP. The Elliptic Restricted Three-Body Problem (ER3BP) introduces a conic motion for the Earth-Moon bodies in the system, resulting in a representative Earth-Moon pulsation. The Bi-Circular Restricted Four-Body Problem (BCR4BP) models the Earth-Moon-Sun system as two nested circular orbits. In the current analysis, the "coherent Sun" refers to a trait in a dynamical model where the motion in Earth-Moon system is explicable via the mutual gravitational interaction of the bodies within the Earth-Moon-Sun three-body system (for graphical illustration for coherency, refer to Park, Sanaga, and Howell [3]). The BCR4BP is known to lack coherency as the Earth-Moon motion remains circular even in the presence of the Sun. The Quasi Bi-Circular Problem (QBCP) introduces the Earth-Moon-Sun motion that follows a periodic solution governed by the three-body problem, resulting in a coherent representation. As a result, the Earth-Moon distance varies over time, but the amplitude of the variation is generally insufficient to fully capture the HFEM behavior [3]. While the Hill Restricted Four-Body Problem (HR4BP) behaves similarly to the QBCP in modeling the Earth-Moon-Sun system, it introduces an additional "Hill approximation" [22], that assumes the solar distance from the Earth-Moon barycenter is sufficiently far ($\rho_S \gg 1$) that enables truncation for the solar gravity term. While within the QBCP, the Earth and Moon affect the solar motion, the Sun remains on a circular motion around Earth-Moon barycenter (B) within the HR4BP. The Hill approximation allows representation of the Earth-Moon motion as a lunar variational periodic orbit within the Hill Restricted Three-Body Problem (HR3BP) [22]. The last two intermediate models in Table 1 are quasi-periodic extensions of the HR4BP. Quasi-periodic motion around the lunar variational periodic orbit is leveraged to supply the basis for the In-plane Quasi-Hill Restricted Four-Body Problem (I-QHR4BP) and the Out-of-plane Quasi-Hill Restricted Four-Body Problem (O-QHR4BP). These models generally introduce the realistic Earth-Moon pulsation and the lunar inclination with respect to the ecliptic (inclined Sun), respectively.[†] Note that all the four-body models introduce a coplanar motion for the Earth-Moon-Sun system except for the O-QHR4BP.

[†]Similar to the ER3BP, there exists some arbitrariness in selecting suitable "eccentricity" and "inclination" values. Refer to Park and Howell [2] as well as Park, Sanaga, and Howell [3] for more discussions.

Table 1: Characteristics of intermediate models (✓: Yes, ✗: No, ?: Ambiguous)

Model	Reference	Earth-Moon Pulsation	Sun	Coherent Sun	Finite Solar Distance	Inclined Sun
ER3BP	[2,23]	✓	✗	N/A		
BCR4BP	[2,24]	✗	✓	✗	N/A	✗
QBCP	[3,25]	?	✓	✓	✓	✗
HR4BP	[3,22]	?	✓	✓	✗	✗
I-QHR4BP	[3]	✓	✓	✓	✗	✗
O-QHR4BP	[3]	?	✓	✓	✗	✓

All dynamical models including the CR3BP, HFEM, and the intermediate models are represented within a common frame and independent variable, as developed in previous investigations [1–3]. The spacecraft position vector within the pulsating-rotating frame is denoted as $\vec{\rho} = x\hat{x} + y\hat{y} + z\hat{z}$. The derivatives of the position vector within the rotating frame are represented as $\dot{\vec{\rho}} = \dot{x}\hat{x} + \dot{y}\hat{y} + \dot{z}\hat{z}$ and $\ddot{\vec{\rho}} = \ddot{x}\hat{x} + \ddot{y}\hat{y} + \ddot{z}\hat{z}$, respectively, where $d(\cdot)/dt = \dot{(\cdot)}$. The equations of motion for the spacecraft within the pulsating-rotating frame result in the following common formulation of differential equations governed by 13 different coefficients, b_{1-13},

$$\ddot{\vec{\rho}}(t) = \begin{bmatrix} b_1 \\ b_2 \\ b_3 \end{bmatrix} + \begin{bmatrix} b_4 & b_5 & 0 \\ -b_5 & b_4 & b_6 \\ 0 & -b_6 & b_4 \end{bmatrix} \dot{\vec{\rho}} + \begin{bmatrix} b_7 & b_9 & b_8 \\ -b_9 & b_{10} & b_{11} \\ b_8 & -b_{11} & b_{12} \end{bmatrix} \vec{\rho} + b_{13} \nabla\Omega, \tag{2}$$

where $\nabla\Omega$ is the gradient of the gravity potential $\Omega = (1-\mu)/\rho_{Ec} + \mu/\rho_{Mc} + \mu_S/\rho_{Sc}$. The quantities $\rho_{Ec}, \rho_{Mc}, \rho_{Sc}$ denote the nd distance from the Earth (E), Moon (M), and Sun (S) to the spacecraft (c). Note that μ_S corresponds to the ratio of the solar mass to the Earth-Moon system mass. Equation (2) delivers a common formulation for different dynamical models encompassed within the hierarchy for application in cislunar space, where each dynamical model supplies different expressions for the coefficients, b_{1-13}, as included in Table 2. In the expressions, the following terms commonly appear: l (Earth-Moon distance), h (Earth-Moon angular momentum vector magnitude), $\vec{A}_{EM}$ (the acceleration vector for the Moon with respect to the Earth), $\vec{J}_{EM}$ (derivative of $\vec{A}_{EM}$ with respect to the dimensional time), and $\vec{B}''$ (the acceleration vector for the Earth-Moon barycenter with respect to an inertially fixed origin). Note that these expressions are measured in dimensional units.

While the derivations for the coefficients b_{1-13} are omitted in the current analysis, relevant details for each dynamical model are noted considering different expressions in Table 2. The different levels of complexity in these expressions result from the different simplifying assumptions employed in each model. For the first three dynamical models (columns 2-4 in Table 2), i.e., the CR3BP, ER3BP, and BCR4BP, the Earth-Moon motion is represented as a conic. This assumption contributes to the simple analytical expressions for the coefficients, b_{1-13}. The eccentricity and true anomaly in the ER3BP are denoted as e and f, respectively. The constant Sun-B distance within the BCR4BP is represented as ρ_{S*}, and θ_S measures the angle between the $\hat{x}$-axis and the solar position vector within xy-plane. In column 5 within Table 2, three types of dynamical models, the (i) QBCP, (ii) (Q)HR4BP, and (iii) HFEM, are included, where the coefficients involve more complex expressions and are instantaneously evaluated. For the periodically perturbed models, i.e., the QBCP and HR4BP, the motion is approximated by a Fourier series with a single frequency [22, 25]. For the quasi-periodically perturbed models under the current investigation, i.e., the QHR4BPs, the coefficients are numerically evaluated along the Earth-Moon motion confined to two-dimensional (2D) invariant tori within the HR3BP [3]. For the HFEM, these quantities are retrieved from the JPL ephemerides, DE 440 [20]. The selection of t, the pulsating time, as the independent variable allows a constant $b_{13} = 1$ across all dynamical models [2]. Lastly, for the models that introduce solar gravity, the evaluation of $\nabla\Omega$ from Eq. (2) requires the instantaneous solar position within the pulsating-rotating frame as defined within each model.

Table 2: Coefficient functions, $b_{1-13}(t)$, for models under investigation [1–3]

b_i	CR3BP	ER3BP	BCR4BP	QBCP/(Q)HR4BP/HFEM	Dominant Freq.
b_1	0	0	$-\frac{\mu_S}{\rho_{S*}^2}\cos\theta_S$	$-\frac{\vec{B}''\cdot\hat{x}}{(t')^2 l}$	ν_2
b_2	0	0	$-\frac{\mu_S}{\rho_{S*}^2}\sin\theta_S$	$-\frac{\vec{B}''\cdot\hat{y}}{(t')^2 l}$	ν_2
b_3	0	0	0	$-\frac{\vec{B}''\cdot\hat{z}}{(t')^2 l}$	$-\nu_2+\nu_3$
b_4	0	$-\frac{e\sin f}{2\sqrt{1+e\cos f}}$	0	$-\frac{2l'}{t'l}-\frac{t''}{t'^2}$	ν_1
b_5	2	$2\sqrt{1+e\cos f}$	2	$\frac{2h}{t'l^2}$	ν_1
b_6	0	0	0	$\frac{2l}{t'h}\vec{A}_{EM}\cdot\hat{z}$	$-\nu_1+2\nu_2$
b_7	1	1	1	$-\frac{l''}{(t')^2 l}+\frac{h^2}{(t')^2 l^4}$	ν_1
b_8	0	0	0	$-\frac{1}{(t')^2 l}\vec{A}_{EM}\cdot\hat{z}$	$2\nu_2$
b_9	1	0	0	$\frac{h'}{(t')^2 l^2}$	$-\nu_1+2\nu_2$
b_{10}	1	1	1	$-\frac{l''}{(t')^2 l}+\frac{h^2}{(t')^2 l^4}+\frac{l^2}{(t')^2 h^2}(\vec{A}_{EM}\cdot\hat{z})^2$	ν_1
b_{11}	0	0	0	$\frac{3hl'-2lh'}{(t')^2 h^2}\vec{A}_{EM}\cdot\hat{z}+\frac{l}{(t')^2 h}\vec{J}_{EM}\cdot\hat{z}$	ν_3
b_{12}	0	$-e\cos f$	0	$-\frac{l''}{(t')^2 l}+\frac{l^2}{(t')^2 h^2}(\vec{A}_{EM}\cdot\hat{z})^2$	ν_1
b_{13}	1	1	1	1	N/A

Frequency Information

The frequency information for various models is reviewed, noting the frequency-based model hierarchy in Fig. 1. The HFEM frequencies are first discussed, followed by the intermediate model frequencies and their capabilities in approximating the respective HFEM frequencies. Gómez, Masdemont, and Mondelo [1] note that the Earth-Moon-Sun HFEM is effectively approximated as a quasi-periodic model governed by five distinct frequencies that are based on Brown's analytical lunar theory. These *basic* frequencies, denoted as ω_{1-5}, are retrieved from the ephemerides DE440 as included in Table 3. For construction of these frequencies, 2^{20} samples are retrieved over the span of years 1550-2550 for the ephemerides, recording the physical quantities as represented in the last column of Table 3; the mean angular rate for the quantities correspond to the frequencies, ω_{1-5}. Note that the frequencies are evaluated differently for t_* and t; the values measured in t are slightly smaller than those in t_*, multiplied by $9.9805\cdot10^{-1}$. For the latter, the relationship dt/dT from Eq. (1) is numerically integrated as retrieval of ephemerides requires the dimensional time. Note that slightly different values for the frequencies appear in the literature [11, 26] that leverage different numerical ephemerides. While coefficients b_{1-13} within the HFEM are approximated as quasi-periodic functions governed by linear, integer combinations of ω_{1-5}, some combinations occur more often than the others and serve as an alternative basis for the frequencies [26]. These *fundamental* frequencies are denoted as ν_{1-5} and are included in Table 4. The linear combinations with respect to the *basic* frequencies (ω_{1-5}) and their values are included along with the physical interpretations. The Earth-Moon distance change (pulsation) is mainly governed by ν_1 that is related to the anomalistic month, i.e., the average time between one lunar perigee to the next. The solar position within the xy-plane in the pulsating-rotating frame is governed by $\nu_2=\omega_2$, also denoted as the synodic month. The next frequency, ν_3, is related to the out-of-plane (z) solar position within the pulsating-rotating frame and denoted as the draconic month. The fourth frequency ν_4 is close to ω_1 that tracks the sidereal

month but offset by ω_5. Similarly, ν_5 is close to ω_2 but apart by ω_5[‡]. The last two frequencies, ν_{4-5}, are typically associated with lower amplitudes within the Fourier representation of the coefficients, b_{1-13}. The most dominant frequencies for the coefficients are included in the last column of Table 2, comprised of the first three fundamental frequencies, ν_{1-3}.

Table 3: Basic frequencies constructed with the ephemerides DE440 [1]

Freq.	Value (nd in t_*)	Value (nd in t)	Interpretation: mean rate of the following quantity
ω_1	1.0000	$9.9805 \cdot 10^{-1}$	Longitude of the Moon
ω_2	$9.2520 \cdot 10^{-1}$	$9.2340 \cdot 10^{-1}$	Elongation of the Moon from the Sun
ω_3	$8.4519 \cdot 10^{-3}$	$8.4354 \cdot 10^{-3}$	Longitude of the lunar perigee
ω_4	$-4.0217 \cdot 10^{-3}$	$-4.0139 \cdot 10^{-3}$	Longitude of the ascending node of the Moon on the ecliptic
ω_5	$6.6892 \cdot 10^{-7}$	$6.6850 \cdot 10^{-7}$	The Sun's longitude of perigee

The capabilities of intermediate models in approximating the HFEM dynamics are intimately linked to the frequency information. Due to the orthogonal nature of the Fourier representation, the intermediate models are expected to only excel in modeling a subset of the variations in b_{1-13} from the HFEM. For example, a periodic intermediate model that incorporates ν_1 succeeds in modeling the variations oscillating with $\nu_1, 2\nu_1, ...$, but faces challenges in approximating other oscillations governed by ν_{2-5}. The frequencies that are introduced in each intermediate model are included in Table 5. Note that the values are determined with respect to the pulsating nd time, t. The ER3BP evaluates the frequency as $\nu_E \approx 0.99943$ nd for the selected eccentricity value of $e = 0.055$ [2]. Note that this value is close to ν_1, but not exact, i.e., $\nu_E > \nu_1$. This discrepancy results from the fact that the ER3BP is incapable of modeling the shift in lunar perigee due to the solar gravity (ω_3) and, thus, the ER3BP does face challenges in accurately modeling the HFEM's ν_1 frequency. Among the periodically perturbed models under investigation, however, the ER3BP is the only option that introduces a realistic Earth-Moon pulsation (Table 1) with a frequency close to ν_1. The periodic four-body problems, i.e., BCR4BP, QBCP, and HR4BP, model the ν_2, or, the synodic frequency. Note that while ν_2 is defined as the same number within the uniform nd time domain, t_*, the value shifts as described in t, and the ν_2 value differs slightly from the HFEM value. Due to the Hill approximations in deriving the HR4BP, the HR4BP introduces $2\nu_2$ as the frequency, rather than ν_2. The physical intuition for this behavior is provided in Park, Sanaga, and Howell [3], where the HR4BP produces more symmetry but "less resolution" for the Earth-Moon-Sun system configuration as compared to the QBCP. The two quasi-periodically perturbed models under the current analysis, i.e., the I-QHR4BP and O-QHR4BP, introduce two frequencies, $\nu_{1,2}$ and $\nu_{2,3}$, respectively. Thus, the I-QHR4BP is capable of modeling the realistic Earth-Moon pulsation, and the O-QHR4BP introduces the lunar inclination with respect to the ecliptic (Table 1) in addition to the solar gravity.

Table 4: Fundamental frequencies for the HFEM [1, 11]

Freq.	Combination	Value (nd in t_*)	Value (nd in t)	Physical meaning
ν_1	$\omega_1 - \omega_3$	$9.9155 \cdot 10^{-1}$	$9.8962 \cdot 10^{-1}$	Anomalistic month
ν_2	ω_2	$9.2520 \cdot 10^{-1}$	$9.2340 \cdot 10^{-1}$	Synodic month
ν_3	$\omega_1 - \omega_4$	1.0040	1.0021	Draconic month
ν_4	$\omega_1 - \omega_5$	1.0000	$9.9805 \cdot 10^{-1}$	$\approx$ Sidereal month
ν_5	$\omega_2 - \omega_5$	$9.2520 \cdot 10^{-1}$	$9.2340 \cdot 10^{-1}$	$\approx$ Synodic month

[‡]While Hou and Liu [11] note that only four independent frequencies exist in a three-body problem due to the azimuthal non-variance in the third-body perturbations, Gómez, Masdemont, and Mondelo [1] demonstrate an accurate representation of a higher-order Fourier approximations of the coefficients b_{1-13} benefits from the fifth frequency, ν_5, likely due to additional perturbations within the HFEM.

Table 5: Frequencies introduced in the intermediate models

Intermediate Model	ER3BP	BCR4BP	QBCP	HR4BP	I-QHR4BP		O-QHR4BP	
Approx. Freq.	ν_1	ν_2	ν_2	$2\nu_2$	ν_1	$2\nu_2$	$2\nu_2$	ν_3
Value (nd in t)	0.99943	0.92520	0.92393	0.92393	0.98955	0.92342	0.92393	1.0026

The frequency information for the Hamiltonian structures are also key. The current investigation focuses on the CR3BP structures and their evolution within different dynamical models. Specifically, the focus is on the Lagrange equilibrium points and Periodic Orbits (POs) within the CR3BP. These structures evolve with 0 and 1 *inherent* frequencies within the pulsating-rotating frame. Such frequencies that are innate to the CR3BP structures are denoted as ν_C. The counterparts within various models are expected to demonstrate (quasi-)periodic behaviors as well [27], while inheriting the model frequency. Thus, the minimum number of frequencies required to describe the analogs in different dynamical models is,

$$n_f = (\#\text{ of fundamental model frequencies}, \nu_{1-5}) + (\#\text{ of inherent CR3BP frequencies}, \nu_C). \quad (3)$$

For example, the Lagrange equilibrium points evolve to periodic orbits ($n_f = 1$) within the periodically perturbed models, and 2D Quasi-Periodic Orbits (QPOs) ($n_f = 2$) within the quasi-periodically perturbed models. Similarly, POs from the CR3BP evolve to 2D QPOs and 3D QPOs ($n_f = 2, 3$) within the periodically and quasi-periodically perturbed models, respectively. The analogs within the HFEM are expected to track multi-dimensional QPOs that inherit ν_{1-5} in addition to the frequency that is inherent to the CR3BP structures. Several numerical methods are employed here to supply and analyze these counterparts.

NUMERICAL METHODS

Differential Correctors

Depending on the expected number of frequencies (n_f) for the counterparts, three different differential correctors are leveraged in the analysis. Detailed implementation of the algorithms may differ for each dynamical model, and it is available in the literature. The strategies employed in this investigation include:

(1) PO targeter ($n_f = 1$): periodic boundary constraints, or, mirror configurations for symmetric orbits, are leveraged to construct POs within the ER3BP [7], BCR4BP [4], QBCP [25], and HR4BP [8].

(2) QPO targeter ($n_f = 2$): the *invariance condition* is targeted leveraging an algorithm developed in Gómez and Mondelo [26] as well as Olikara and Scheeres [28], applied for construction of 2D QPOs in the ER3BP [21], BCR4BP [29], QBCP [30], HR4BP [5], and QHR4BPs [3].

(3) Multi-Year Trajectory (MYT) targeter ($n_f \geq 3$): for cases where the expected frequencies are greater than or equal to three, the computational costs to construct accurate Hamiltonian structures become intractable. Rather, a continuous trajectory is constructed over a sufficiently long time horizon to uncover the underlying multi-dimensional quasi-periodic motion, originating from the CR3BP structure as the initial guess. As the boundary conditions are not enforced, the differential corrector results in an underdetermined system [13], where a minimum-norm solver is leveraged to locate a continuous trajectory that is in the vicinity of the CR3BP initial guess. An example is provided for the HFEM [21] and is applied for the QHR4BPs and HFEM in the current investigation where $n_f \geq 3$. For the *long* time horizon, 20 years is selected as it surpasses the Saros period (18.04 years) [25]. This period covers near-resonant revolutions of the sidereal, synodic, and draconic months; thus, it is assumed that the perturbations from ν_{1-3} are sufficiently captured over 20 years (Table 4).

Fourier Analysis Tools

Fourier analysis provides a concrete tool to characterize the gap between the CR3BP and HFEM to aid in gauging the capabilities of different intermediate models. A general objective is extracting the frequencies from solutions originating in different dynamical models and representing them as linear combinations of the fundamental frequencies, ν_{1-5}, as well as the CR3BP frequency that is inherent to the structure, ν_C. Then, counterparts from different models are compared in terms of the *matched* frequency structure.

For accurate detection of the frequencies as well as the amplitudes for a given trajectory, the collocation refinement method as discussed in Gómez, Mondelo, and Simó [31] is leveraged. The algorithm searches for a quasi-periodic approximation given an input Discrete Fourier Transform (DFT) signal as,

$$Q_{\mathtt{f}}(t) = A_0 + \sum_{i=1}^{N} A_i \cos(\mathtt{f}_i t) + B_i \sin(\mathtt{f}_i t), \tag{4}$$

where N is the user input for the maximum number of investigated frequencies. The approximated frequencies $\mathtt{f}_i$ (not to be confused with f, the true anomaly for the ER3BP) are arranged in a decreasing order with respect to the amplitude of the oscillation, i.e., $\sqrt{A_i^2 + B_i^2}$. The method in Gómez, Mondelo, and Simó [31] leverages a set of collocation conditions to sequentially refine $A_0, A_i, B_i, \mathtt{f}_i (1 \leq i \leq N)$ by solving a square system of linear equations. Throughout the current investigation, the signals are constructed at 2^{16} sample times, evenly placed over a span of 20 years; note that the times are linearly spaced in terms of the pulsating time, t. The signals under consideration are x- and z-position components along the trajectories. While an infinite number of frequencies $\mathtt{f}_i$ are required to accurately track the given quasi-periodic function, the trajectories under investigation display a regular behavior where the amplitudes decrease for higher frequencies; thus, the lower-frequency domain information is the most significant; the first ten dominant frequencies for a given signal are investigated by default in the current analysis ($N = 10$). For the Multi-Year Trajectory (MYT) solutions, the first and last year along the solution is discarded as it likely displays more chaotic behavior [10] due to the lack of boundary constraints.

The frequency structures corresponding to the frequencies $\mathtt{f}_i$ emerge by approximating them as linear, integer combinations of ν_{1-5} as well as ν_C [1]. For the intermediate models, only a subset of the fundamental frequencies is incorporated into this process. For example, for the ER3BP, $\mathtt{f}_i$ is approximated as a linear, integer combination of $0.99943 \approx \nu_1$ from Table 5 and ν_C. For investigation of the HFEM analogs, only the first four fundamental frequencies, i.e., ν_{1-4}, are incorporated as the influence from ν_5 is expected to be negligible [1] and the difference between ν_2 and ν_5 is on the order of 10^{-7} nd that is too small to be accurately detected.

RESULTS 1: LAGRANGE EQUILIBRIUM POINT COUNTERPARTS

Collinear Lagrange Points: L_{1-3}

The counterparts for the collinear Lagrange points, i.e., L_{1-3}, are constructed in various models and compared. The geometry of the analogs is depicted in Figs. 2 and 3, and the corresponding frequency information is provided in Table 6. The HFEM analogs for the L_{1-3} are investigated by multiple authors [10, 12, 13]. While these previous investigations employ different numerical strategies to compute long-range HFEM counterparts, they all report consistent behaviors. Such results are recreated and plotted in blue within Fig. 2 over 20 years. The position projection on the xy-plane is plotted in Figs. 2(a), 2(c), 2(e). Note that many intermediate models under consideration admit equilibrium collinear Lagrange points even in the presence of the perturbations in addition to the CR3BP. As demonstrated in Park, Sanaga, and Howell [3], the collinear Lagrange points remain *analytical* equilibrium points within the ER3BP as well as (Q)HR4BP; these intermediate models face challenges in approximating the variations observed from the HFEM Lagrange point counterparts. This nature is straightforwardly apparent in the ER3BP given the form of the coefficients within Table 2. For the (Q)HR4BP, the Hill approximation supplies zero net perturbing accelerations for the collinear Lagrange points, even in the presence of the solar gravity. Indeed, the QBCP serves as the only intermediate model (under consideration) that reasonably approximates the behaviors observed within the HFEM. The QBCP counterparts for L_1 and L_3 are very closely approximating the HFEM analogs, while L_2 counterpart within the QBCP displays a smaller variation in comparison to the HFEM (Figs. 2(a), 2(c), 2(e)). As the QBCP models the Sun-Earth-Moon system within a common plane, it does not introduce any z-component variation for the Lagrange point counterparts, as is obvious from Figs. 2(b), 2(d), 2(f). The counterparts within the BCR4BP are provided separately in Fig. 3 for the L_1 and L_3, as the size of the analogs is much larger compared to other models from Fig. 2. The L_2 counterpart does not exist within the BCR4BP as discussed in Jorba-Cuscó, Farrés, and Jorba [32]. It is notable that, due to the lack of coherency, the variations in the

$L_{1,3}$ geometry within the BCR4BP do not bridge the gap between the CR3BP and HFEM. Not surprisingly, the models under consideration are incapable of introducing z-direction variations as observed in the HFEM analogs.

The geometry observations are confirmed within the frequency domain as illustrated in Table 6. For each collinear Lagrange point, the first three dominant frequencies within the HFEM ($\mathtt{f}_i$ from Eq. (4)) are represented as linear combinations of ν_{1-4}. Note that the inherent CR3BP frequency, ν_C, does not appear as the Lagrange point is an equilibrium point within the CR3BP. The corresponding amplitudes ($\sqrt{A_i^2 + B_i^2}$) are also included. The capability of the QBCP in approximating the HFEM is evident for $L_{1,3}$, where the most dominant frequency and the corresponding amplitude are also located within the QBCP. The relatively poor performance for the L_2 is also observed from the frequency structure, where the most dominant frequency for the HFEM involves both ν_1 and ν_2; the QBCP cannot model ν_1-induced perturbations. The limitations of the BCR4BP are also illustrated within the frequency domain, where it provides (i) amplitudes that are too large, but also, (ii) the incorrect frequency structure, i.e., $2\nu_2$, that does not match the HFEM frequency, $3\nu_2$. Note that as the other models, e.g., the HR4BP, supply equilibrium points, their frequency structures are not analyzed.

While the collinear Lagrange points are non-generic CR3BP structures as the regions are characterized by extremely low velocity and acceleration within the pulsating-rotating frame, they present an interesting case for investigating the model hierarchy within cislunar space. Even though different intermediate models *do introduce* additional components as compared to the CR3BP and displayed in Table 1, the additional information does not always guarantee a "better prediction" of the geometry change for the CR3BP structures within the HFEM. Rather, the performance depends on the region within cislunar space as well as the assumptions introduced for each intermediate dynamical model.

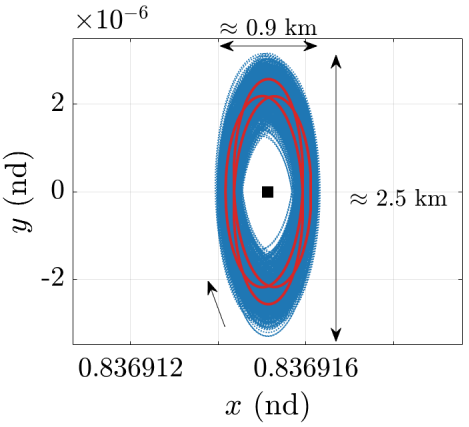

(a) L_1: xy-projection

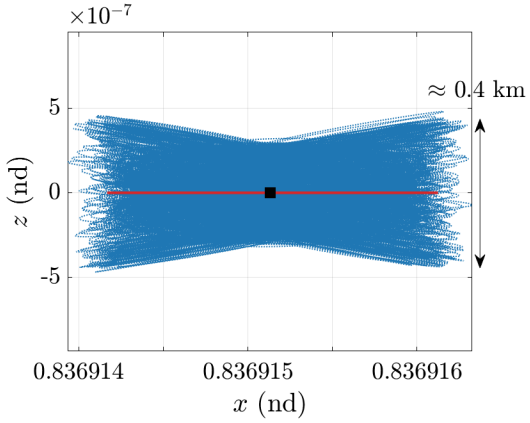

(b) L_1: xz-projection

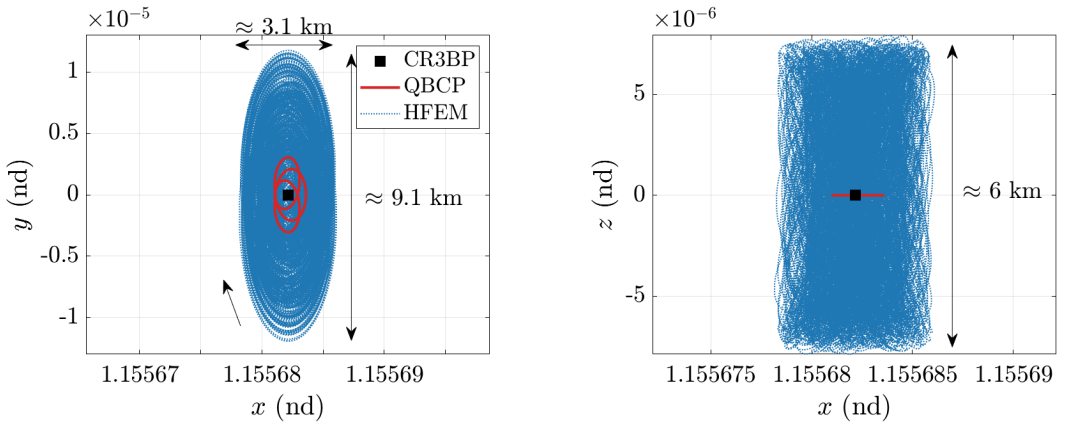

(c) L_2: xy-projection

(d) L_2: xz-projection

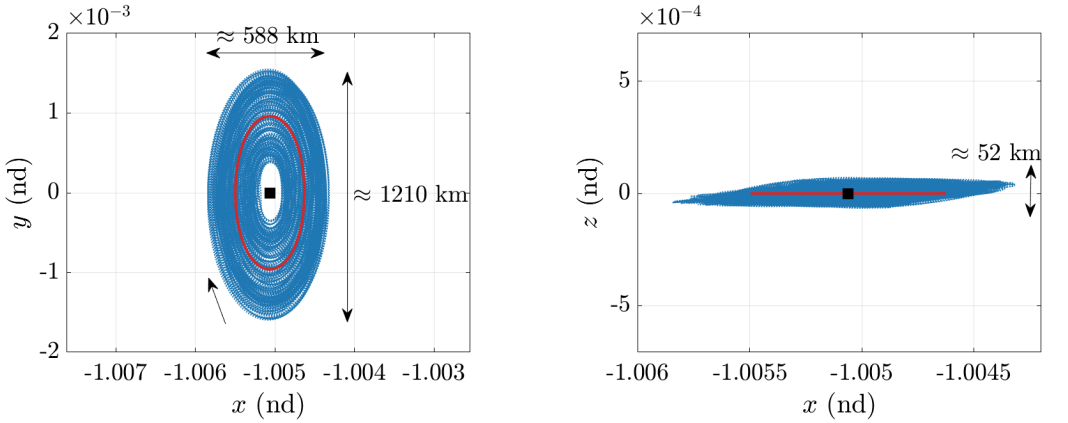

(e) L_3: xy-projection

(f) L_3: xz-projection

Fig. 2: Collinear Lagrange point counterparts for the HFEM (blue), QBCP (red), and the rest (black square)

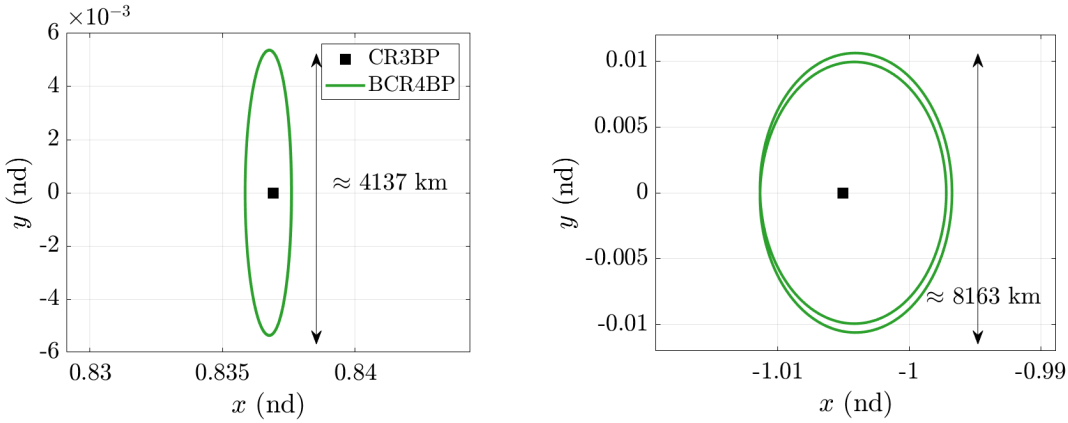

(a) L_1 xy projection

(b) L_3 xy projection

Fig. 3: Collinear Lagrange point BCR4BP counterpart: position components projection

Table 6: Frequency structure for the collinear Lagrange points: x-position component

	Model	Amplitude (nd)	ν_1	ν_2	ν_3	ν_4
L_1	HFEM	$\mathbf{8.5590 \cdot 10^{-7}}$	0	**3**	0	0
		$1.2349 \cdot 10^{-7}$	0	1	0	0
		$8.6188 \cdot 10^{-8}$	0	4	0	-1
	QBCP	$\mathbf{8.5331 \cdot 10^{-7}}$	N/A	**3**	N/A	N/A
	BCR4BP	$8.7424 \cdot 10^{-4}$	N/A	2	N/A	N/A
L_2	HFEM	$1.6424 \cdot 10^{-6}$	-1	3	0	0
		$\mathbf{1.1529 \cdot 10^{-6}}$	0	**3**	0	0
		$9.9654 \cdot 10^{-7}$	1	0	0	0
	QBCP	$\mathbf{1.1079 \cdot 10^{-6}}$	N/A	**3**	N/A	N/A
	BCR4BP	N/A	N/A	N/A	N/A	N/A
L_3	HFEM	$\mathbf{4.4019 \cdot 10^{-4}}$	0	**1**	0	0
		$1.7452 \cdot 10^{-4}$	0	0	0	1
		$4.1177 \cdot 10^{-5}$	0	2	0	-1
	QBCP	$\mathbf{4.4311 \cdot 10^{-4}}$	N/A	**1**	N/A	N/A
	BCR4BP	$7.1954 \cdot 10^{-3}$	N/A	2	N/A	N/A

Triangular Lagrange Point: L_4

Considering the mirror configuration between the L_4 and L_5 points, the current investigation only discusses the counterparts for the L_4 point in different dynamical models. First, the ER3BP supplies an equilibrium L_4 point and is not considered here. The counterparts as constructed in other dynamical models are plotted together in Fig. 4(a), illustrating the xy-projection. The periodically perturbed four-body problems that include the Sun in the model admit a periodic motion for the L_4 counterpart. The geometries for the counterparts are closely depicted in Fig. 4(b). While the size of the analogs within the BCR4BP, QBCP, HR4BP is very similar within the xy-plane, the structures track slightly different behaviors. Note that the HR4BP has one loop structure from the fact that the fundamental frequency is $2\nu_2$ rather than ν_2. The other two four-body models supply two-loop PO structures. The BCR4BP supplies a distinct geometry as opposed to the other four-body models; this property is also related to the lack of coherency. The two quasi-periodic dynamical models, QHR4BPs, demonstrate distinct behaviors. The O-QHR4BP counterpart (2D QPO) produces nearly identical results within the xy-plane as compared to the HR4BP; two plots are almost indistinguishable within Fig. 4(b). The zoomed out view in Fig. 4(a) displays two large trajectories that emerge in the I-QHR4BP and the HFEM. The frequency structures for the x-position component from Table 7 confirms these observations. Note that the first dominant frequency within the HFEM involves both ν_1 and ν_2. The perturbation corresponding to this frequency is only expected to be modeled within the I-QHR4BP and, thus, the I-QHR4BP is capable of modeling the xy-projection variations better than other intermediate models. The QBCP, BCR4BP, and O-QHR4BP introduce $2\nu_2$ as the dominant frequency where the associated amplitudes are consistently evaluated across these models. Note that the amplitude values are slightly smaller as compared to the respective HFEM value; such discrepancies potentially imply that the t variable as defined from Eq. (1) is inadequate for describing the dynamics around L_4; however, future research is warranted to confirm this insight. The BCR4BP supplies a much smaller amplitude for the $2\nu_2$ frequency, explaining the slightly

small size for the BCR4BP analog in Fig. 4(b). The fact that the BCR4BP behaves qualitatively different from other coherent four-body models potentially indicates a challenge in employing this model for bridging the gap between the CR3BP and HFEM throughout the Earth-Moon interior region.

While the in-plane (xy) geometry for the L_4 counterparts behave predictably within the HFEM, more diverse behaviors are reported for the z-direction position components. For example, Gómez et al. [19] record multiple HFEM L_4 counterparts with varying z-amplitudes between ≈ 0.001 and ≈ 0.006 nd. These values are smaller than the values supplied by Hou and Liu [11], who report 0.02 nd as the amplitude associated with the z-direction oscillations. Such an arbitrary behavior is explained via the O-QHR4BP that introduces ν_2 as well as ν_3; the other intermediate models introduce the coplanar Earth-Moon-Sun motion, and do not offer sufficient insights into the z-direction behaviors for the HFEM counterparts.

The complexity of the L_4 countepart within the HFEM is partially explained by the near-resonant behavior within the O-QHR4BP. The linear stability information for the CR3BP and the HR4BP L_4 structures are briefly reviewed. The L_4 Lagrange point in the CR3BP allows a center$\times$center$\times$center linear stability structure, where the two in-plane center subspaces lead to the short-period and long-period orbits around L_4. The out-of-plane direction center subspace allows the vertical orbits. For the L_4 counterpart PO within the HR4BP, one of the in-plane (short-period) center subspaces and the out-of-plane center subspace persist [33]; the latter is associated with a pair of eigenvalues of $\lambda_v \approx 0.86015 \pm 0.51004j$, evaluated over one synodic period, where $j^2 = -1$. Denote the frequency associated with this eigenvalue as ν_v, corresponding to the vertical orbit. On a different note, the O-QHR4BP introduces the frequency ν_3 in addition to the HR4BP. The value for ν_3 within the O-QHR4BP evolves *nonlinearly* with the lunar inclination with respect to the ecliptic, where in the limiting case, it approaches the value provided by the out-of-plane direction eigenvalue within the HR3BP, evaluated for the lunar varitional periodic orbit [3]. The value is supplied as $\lambda_3 = 0.86019 \pm 0.50100j$. Note that $\lambda_3 \approx \lambda_v$, $\nu_3 \approx \nu_v$ [11]; the two values are almost in $1:1$ resonance, and QPO structures originating from these two center modes may be located in a close vicinity in the O-QHR4BP. Interestingly, such a behavior is indeed observed in the O-QHR4BP. The true L_4 counterpart within the O-QHR4BP is expected to track a 2D QPO. Leveraging the HR4BP L_4 counterpart (PO) as the initial guess, one 2D QPO branch is initially revealed. The corresponding hodograph is plotted as blue markers in Fig. 5(a). The horizontal axis depicts the maximum z-component along the trajectory, and the vertical axis corresponds to the lunar inclination value as introduced by O-QHR4BP models with different i values, until it reaches the desired value at $i \approx 5.14^\circ$ [3]. Following this original branch (blue in Fig. 5(a)), however, the z_{max} value rapidly increases and the QPO targeting algorithm fails to accurately represent the complex shape of the invariant curve. Note that along this hodograph, the z_{max} value is far larger than 0.02 nd, a value reported in Hou and Liu [11], implying that the structures located by previous authors are not leveraging the structures along the blue hodograph. Employing different step sizes within the differential corrector, a different branch is located, colored in red within Fig. 5(a). This branch is denoted as "resonant" as $\nu_3 = \nu_v$ is satisfied along the family. While this different branch indeed tracks 2D QPO motion, the origin of the structure is located at a HR4BP 2D QPO that incorporates $2\nu_2$ and $\nu_v = \nu_3$ as the frequencies. The vertical 2D QPO family within the HR4BP is reported in Peterson et al. [33], where one member with the resonance condition ($\nu_3 = \nu_v$) is marked with the magenta star in Fig. 5(a). This branch continues to the desired inclination at $i \approx 5.14^\circ$. Note that the blue and red branches are distinct; for illustration, consider two different QPOs constructed at the O-QHR4BP with $i \approx 3.20^\circ$ in Fig. 5(b).

While the two branches partially explain the diverse behaviors in the z-direction observed within the HFEM, it still does not fully capture the behaviors reported in previous literature. For example, at the end of the red hodograph, $z_{max} \approx 0.007$, a value that falls short of the value reported in Hou and Liu [11]. Such a discrepancy is potentially explained via the sensitivity of the z-amplitude from nearby 3D QPOs within the O-QHR4BP. Note that within the HR4BP, the center manifold corresponding to the short-period motion persists. It is possible that the O-QHR4BP structures that are not precisely located on the two 2D QPO branches as displayed in Fig. 5(a), actually leverage the 3D QPOs, altering the z_{max} values. To confirm this insight, Multi-Year Trajectory (MYT) solutions are constructed within the O-QHR4BP. Originating from the 2D QPO solution at the end of the resonant branch (red in Fig. 5(a)), continuous solutions over 20 year are constructed while controlling the z_{max} values. Some of these MYT solutions are illustrated as grey stars in

Fig. 5(a). The corresponding geometries for various z_{max} values are provided in Fig. 6(a), where Fig. 6(b) illustrates the position crossings at the hyperplane where $y = \sqrt{3}/2, \dot{y} < 0$. Note that long range solutions are easily constructed for different z_{max} values, suggesting the existence of nearby 3D QPOs. Interestingly, however, the crossings at the hyperplane indicate nearly 2D QPO behavior, where, the "width" for the crossings do not significantly increase with varying z_{max}. This numerical experiment implies that, by stepping a small amount into the short-period center mode, large variations within the z_{max} occur.

This information from the O-QHR4BP is extrapolated to the HFEM L_4 structures. Within Fig. 7, five different HFEM L_4 counterpart trajectories are constructed that are associated with varying z-amplitudes over 20 years. All of these trajectories share the common frequency structure within the x-position as included in Table 7, and hence, the trajectories are more extended within the xy-plane as opposed to the O-QHR4BP structures. However, the most dominant frequency for the z-position in these HFEM counterparts all track ν_3, the frequency modeled within the O-QHR4BP. Thus, the varying z-amplitude solutions from the O-QHR4BP (that often leverages a 3D QPO motion) provides foundational structures for the various HFEM behaviors near L_4. These diverse nearby structures hinder the identification of a "true" L_4 counterpart within the HFEM.

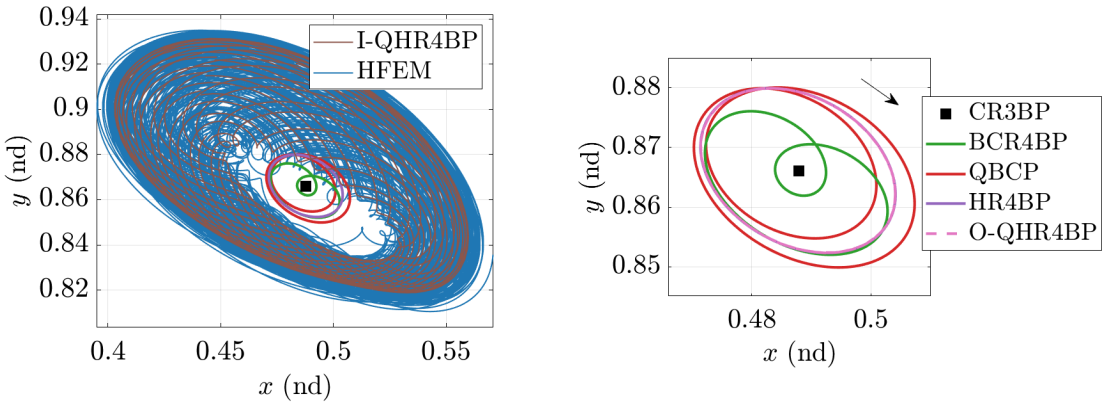

(a) Zoomed out view

(b) Zoomed in view

Fig. 4: L_4 counterparts, xy-projection

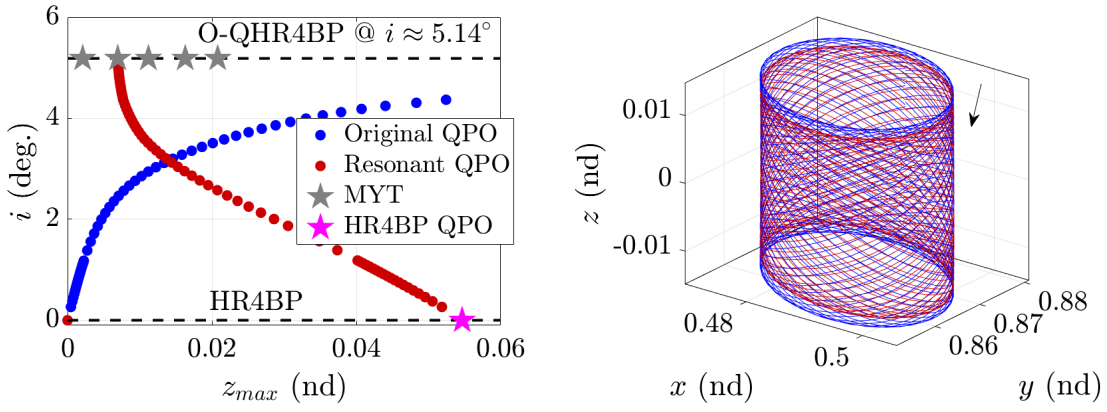

(a) Hodographs

(b) Two different QPOs at $i \approx 3.20°$

Fig. 5: L_4 2D QPO families within the O-QHR4BP with varying inclinations

Table 7: Frequency structure for the L_4 Lagrange points: x-position component

	Amplitude (nd)	ν_1	ν_2	ν_3	ν_4
HFEM	$5.7759 \cdot 10^{-2}$	-1	2	0	0
	$1.8221 \cdot 10^{-2}$	0	2	0	0
	$1.3267 \cdot 10^{-2}$	1	0	0	0
QBCP	$1.6365 \cdot 10^{-2}$	N/A	2	N/A	N/A
BCR4BP	$9.3820 \cdot 10^{-3}$	N/A	2	N/A	N/A
HR4BP	$1.6365 \cdot 10^{-2}$	N/A	2	N/A	N/A
I-QHR4BP	$5.6577 \cdot 10^{-2}$	-1	2	N/A	N/A
	$1.8210 \cdot 10^{-2}$	0	2	N/A	N/A
	$1.3060 \cdot 10^{-2}$	1	0	N/A	N/A
O-QHR4BP	$1.6301 \cdot 10^{-2}$	0	2	N/A	N/A

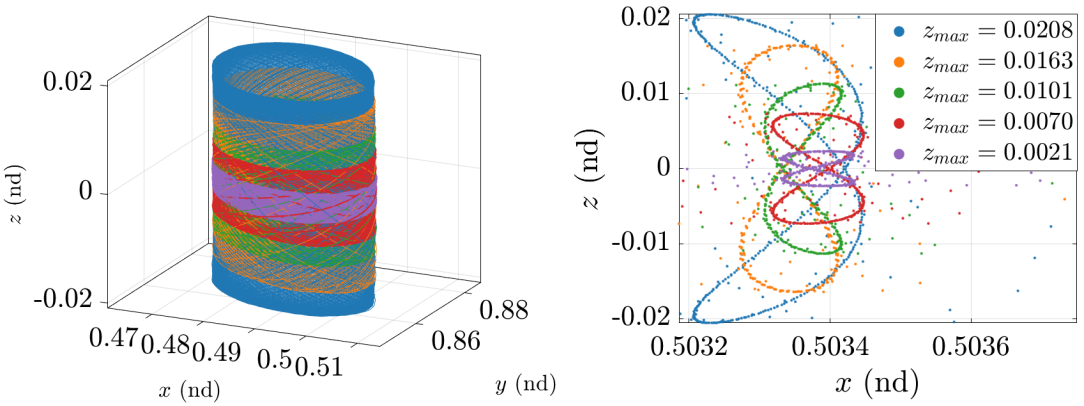

(a) Geometry within the pulsating-rotating frame

(b) Crossing at $y = \sqrt{3}/2$, $\dot{y} < 0$

Fig. 6: O-QHR4BP Multi-Year Trajectory (MYT) over 20 years with varying z-amplitudes

RESULTS 2: PERIODIC ORBITS IN THE LUNAR VICINITY

Various CR3BP PO structures and their analogs are investigated within the lunar vicinity considering their relevance for future space missions. In Fig. 8(a), five CR3BP POs are selected: Lyapunov orbits around $L_{1,2}$, one L_1 northern halo orbit, one L_2 southern halo orbit, and a Distant Retrograde Orbit (DRO). These structures are selected such that ν_C, the frequency for the CR3BP period is not in resonance with ν_{1-4} to avoid (i) numerical complexities with discerning ν_C from ν_{1-4} and (ii) falling into the HFEM local basin characterized by the resonant tori [10]; the frequencies ν_C for each orbit are included in Table 8. The HFEM MYT solutions corresponding to the selected CR3BP POs are plotted in Fig. 8(b). The analogs within various intermediate models are also retrieved leveraging the QPO targeter for the periodically perturbed models ($n_f = 2$) and the MYT targeter for the quasi-periodically perturbed models ($n_f = 3$). The numerical targeters are able to produce counterparts for various models except for following two cases: (i) L_2 Lyapunov and (ii) L_2 halo QPOs in the BCR4BP. Further investigations are required to confirm the cause for the numerical challenge that remains out-of-scope for the current analysis; these two cases are omitted here.

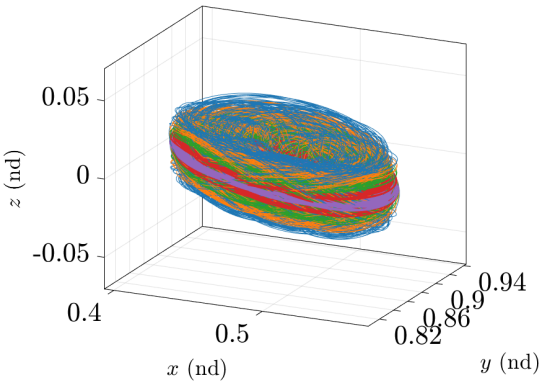

Fig. 7: HFEM Multi-Year Trajectory (MYT) over 20 years with varying z-amplitudes

Table 8: Selected CR3BP POs

Orbit	L_1 Lyapunov	L_2 Lyapunov	L_1 Halo	L_2 Halo	DRO
ν_C (nd in t)	2.1666	1.8212	2.2848	1.8984	3.9270
Period (days)	12.61	15.00	11.96	14.39	6.96

The frequency structures for the HFEM counterparts are analyzed by identifying patterns associated with the first few dominant frequencies. Observe that the HFEM analogs are expected to introduce linear, integer combinations of ν_C as well as ν_{1-4}. Depending on these frequencies, different patterns emerge; distinctly colored markers are assigned for patterns as in Table 9. The CR3BP PO frequency is assigned the black color, corresponding to (0, 0, 0) in terms of the RGB color code. Then, colors red, green, blue, are assigned to the perturbing frequencies, ν_{1-3}, respectively. For examples, frequency structures that involve ν_1, and also potentially ν_C, but does not include ν_{2-3}, is represented as red (1, 0, 0). The frequency structure that allows a convolution of ν_{1-3} is associated with a color code that is added from ν_{1-3}. For example, the frequency structure that involves both ν_{1-2} but not ν_3 are assigned yellow (1, 1, 0) that combines red (1, 0, 0) and green (0, 1, 0) from ν_1 and ν_2, respectively. Utilizing this color scheme, the frequency structures for various HFEM counterparts are plotted in Figs. 9 and 10 for the x- and z-position components, respectively. The x-position frequency structures display similar behaviors across different orbits. The black star dominates the amplitude as the HFEM structure is constructed in the vicinity of the underlying CR3BP periodic motion and, thus, the most impactful frequency corresponds to the ν_C, often followed by multiples of ν_C. The most dominant *perturbing* frequency for these structures is ν_1, associated with the Earth-Moon pulsation [2]. The perturbations from ν_2 appear to be secondary as compared to ν_1, followed by convoluted frequencies between ν_{1-2} and ν_{2-3}. The z-direction components display a more diverse behavior. For the planar orbits, i.e., the Lyapunovs and DRO, it is expected that the z-direction perturbations within the HFEM are introduced by the inclined Sun, or, ν_3. The markers often demonstrate convoluted frequencies between $\nu_{1,3}$ or $\nu_{2,3}$. Note that the third dominant frequency for the DRO in the z-direction is blank as it involves ν_4 and cannot be represented in markers from Table 9. For the halo orbits that already include out-of-plane components, ν_1 emerges as the most dominant perturbing frequency again.

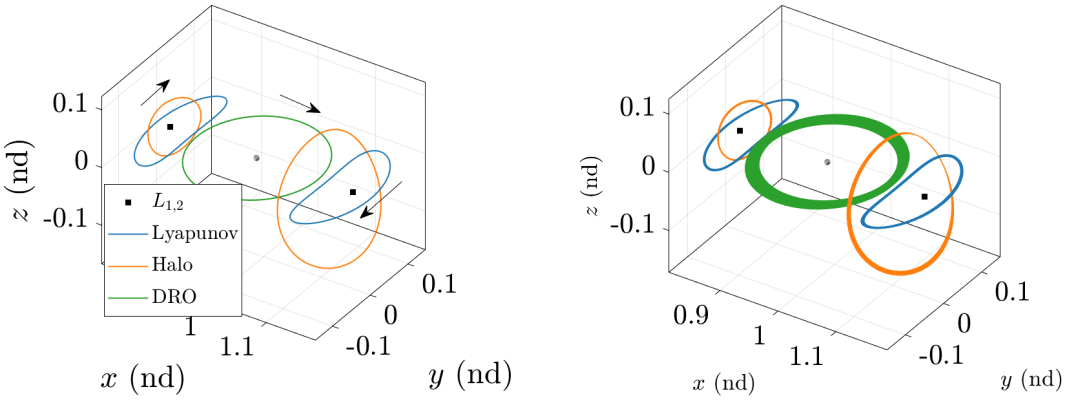

(a) Selected CR3BP POs

(b) HFEM analogs over 20 years

Fig. 8: Selected CR3BP POs in the lunar vicinity and their counterparts within the HFEM

Table 9: Frequency patterns and assigned markers in Figs. 9 and 10

Frequency pattern	ν_C	$\nu_{C,1}$	$\nu_{C,2}$	$\nu_{C,3}$	$\nu_{C,1,2}$	$\nu_{C,1,3}$	$\nu_{C,2,3}$	$\nu_{C,1-3}$
RGB color code	(0, 0, 0)	(1, 0, 0)	(0, 1, 0)	(0, 0, 1)	(1, 1, 0)	(1, 0, 1)	(0, 1, 1)	(1, 1, 1)
Markers (Figs. 9 & 10)	★	★	★	★	★	★	★	★

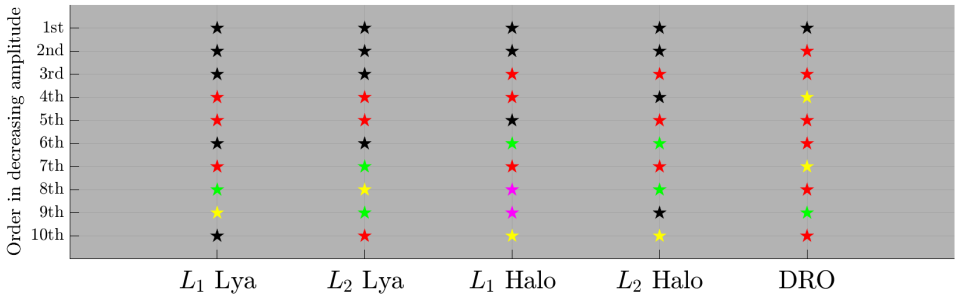

Fig. 9: HFEM counterparts' frequency structure for x-position components

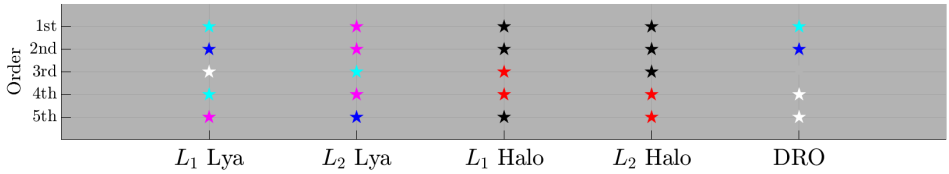

Fig. 10: HFEM counterparts' frequency structure for z-position components

The frequency structures for the counterparts within various models are analyzed and juxtaposed with the HFEM results. Five different plots are included in Fig. 11 for each PO. The different colorbars represent intermediate models as well as the HFEM as labeled in Fig. 11(f). The horizontal axis of the plots display the log_{10} value of the nd amplitude associated with each frequency. The vertical axis lists the dominant *perturbing* frequencies as demonstrated in Figs. 9 and 10. For example, for the L_1 Lyapunov orbit, five

different perturbing frequencies exist for the x-position and are included in the vertical axis of Fig. 11(a). The perturbing frequencies within the z-position component are also included on the same axis; however, the ones that are not expected in any of the intermediate models are omitted for brevity, e.g., $\nu_1 + \nu_3$. The horizontal black lines in Fig. 11(a) separate each perturbing frequency. Then, the capabilities and limitations of different intermediate models in approximating the components from the HFEM are straightforwardly analyzed from the bar graphs. For example, note $x_{4th} = \nu_C + \nu_1$ that appears as the first perturbing frequency for the L_1 Lyapunov analog within the HFEM. It is visually clear that the intermediate models that approximately introduce ν_1, i.e., the ER3BP and I-QHR4BP, excel in approximating the amplitude. Such amplitudes are not approximated in any other intermediate models as expected.

Overall, the frequency information is well-matched across various CR3BP PO structures in the lunar vicinity. The variations that are captured in the intermediate models realistically approximate the HFEM behavior for the same frequency structure. Notable exceptions occur for the BCR4BP, where the amplitudes corresponding to the same frequency are mismodeled within the BCR4BP, e.g., the green bar for x_{6th} in Fig. 11(c). Counterparts within various models are examined for the L_1 halo orbit at the hyperplane constructed at $z = 0, \dot{z}$ in Fig. 12. Note that all dynamical models except for the BCR4BP are closely grouped (the crossings from HR4BP and O-QHR4BP are closely located from the QBCP and cannot be discerned from the view) as in Fig. 12(a). Zooming out, however, note that the BCR4BP L_1 halo counterpart QPO is distant from the other structures, also confirmed by the qualitatively different frequency structure in Fig. 11(c).

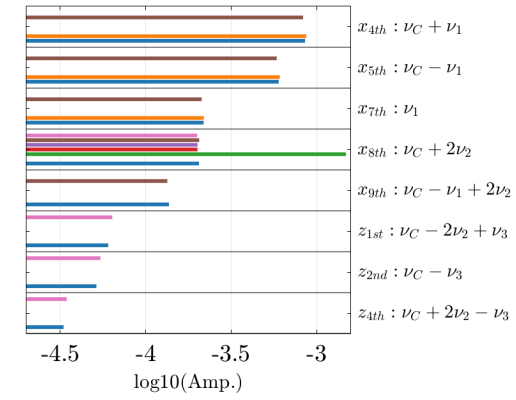

(a) L_1 Lyapunov

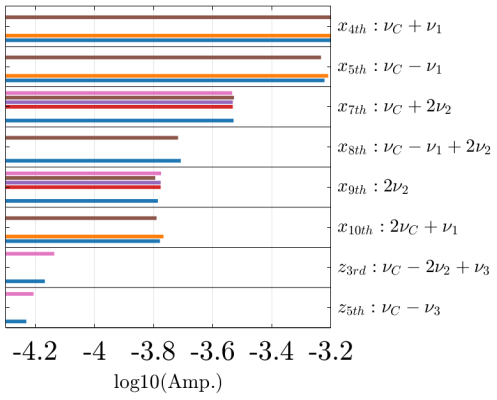

(b) L_2 Lyapunov

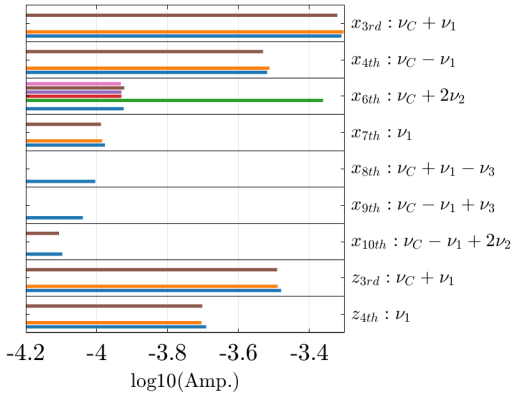

(c) L_1 halo

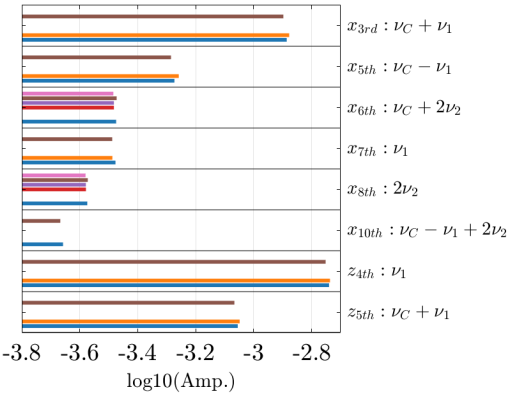

(d) L_2 halo

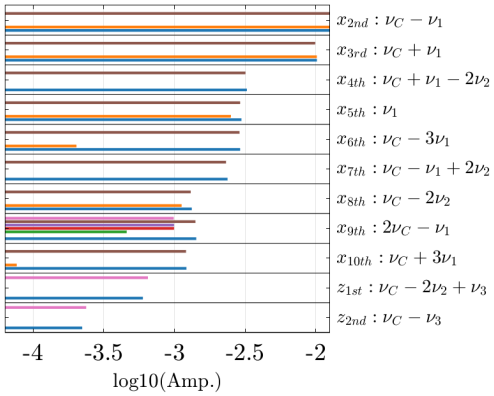

(e) DRO

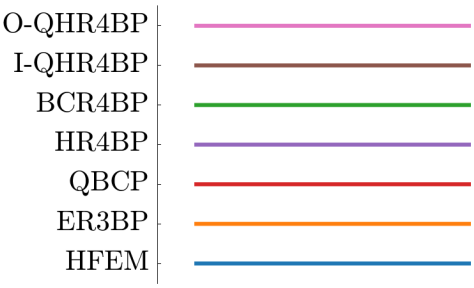

(f) Legend

Fig. 11: Frequency structure for the selected POs focusing on the perturbing frequencies

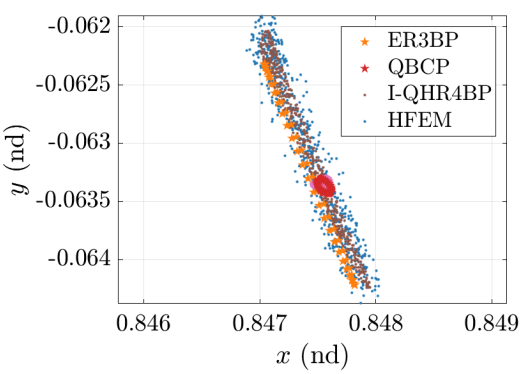

(a) Zoomed in view

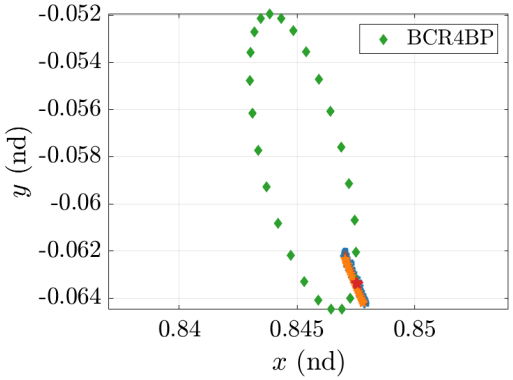

(b) Zoomed out view

Fig. 12: Crossings for L_1 halo at $z = 0, \dot{z} > 0$

CONCLUDING REMARKS

A frequency-based model hierarchy within the cislunar domain is numerically investigated for multiple Circular Restricted Three-Body Problem (CR3BP) structures. The analogs for the structures are refined within various intermediate models as well as a Higher-Fidelity Ephemeris Model (HFEM). The evolution of the geometry of CR3BP structures within a common rotating frame is investigated with Fourier analysis. The frequency structures for the analogs in various models are analyzed, recognizing the distinct frequency patterns and their respectively amplitudes. The analysis offers some insight into the relative importance of perturbations associated with distinct frequencies for sample structures and serves as an initial step in constructing a suitable model hierarchy across the cislunar domain.

ACKNOWLEDGEMENTS

Valuable discussions with members from Multi-Body Dynamics Research Group are appreciated. Beom Park would like to thank Kwanjeong Educational Foundation for the financial support. Rohith Reddy Sanaga would like to thank Department of Computer Science Department at Purdue University. Portions of this work are also supported by Purdue University and NASA JSC.

REFERENCES

[1] G. Gómez, J. J. Masdemont, and J.-M. Mondelo, "Solar system models with a selected set of frequencies," *Astronomy & Astrophysics*, Vol. 390, No. 2, 2002, doi:10.1051/0004-6361:20020625.

[2] B. Park and K. C. Howell, "Assessment of dynamical models for transitioning from the Circular Restricted Three-Body Problem to an ephemeris model with applications," *Celestial Mechanics and Dynamical Astronomy*, Vol. 136, No. 6, doi:10.1007/s10569-023-10178-9.

[3] B. Park, R. R. Sanaga, and K. C. Howell, "A frequency-based hierarchy of dynamical models in cislunar space: leveraging periodically and quasi-periodically perturbed models.," *Celestial Mechanics and Dynamical Astronomy*, Vol. 137, No. 5, doi:10.1007/s10569-025-10236-4.

[4] K. K. Boudad, K. C. Howell, and D. C. Davis, "Dynamics of synodic resonant near rectilinear halo orbits in the bicircular four-body problem," *Advances in Space Research*, Vol. 66, No. 9, 2020, doi:10.1016/j.asr.2020.07.044.

[5] D. B. Henry, J. J. Rosales, G. M. Brown, and D. J. Scheeres, "Quasi-periodic orbits around Earth-Moon L_1 and L_2 in the Hill restricted four-body problem," *AAS/AIAA Astrodynamics Specialist Conference, Big Sky, Montana, August 13-17, 2023.*,

[6] J. J. Rosales, A. Jorba, and M. Jorba-Cuscó, "Families of Halo-like invariant tori around L_2 in the Earth-Moon Bicircular Problem," *Celestial Mechanics and Dynamical Astronomy*, Vol. 133, No. 4, 2021, doi:10.1007/s10569-021-10012-0.

[7] H. Peng and S. Xu, "Stability of two groups of multi-revolution elliptic halo orbits in the elliptic restricted three-body problem," *Celestial Mechanics and Dynamical Astronomy*, Vol. 123, No. 3, 2015, doi:10.1007/s10569-015-9635-2.

[8] R. R. Sanaga and K. Howell, "Analyzing the Challenging Region in the Earth-Moon L_2 Halo Family via Hill Restricted Four-Body Problem Dynamics," *AIAA SCITECH 2024 Forum*, doi:10.2514/6.2024-1451.

[9] L. T. Peterson, J. J. Rosales, and D. J. Scheeres, "The vicinity of Earth–Moon L_1 and L_2 in the Hill restricted 4-body problem," *Physica D: Nonlinear Phenomena*, Vol. 455, 2023, doi:10.1016/j.physd.2023.133889.

[10] Y. Lian, G. Gómez, J. J. Masdemont, and G. Tang, "A note on the dynamics around the lagrange collinear points of the earth–moon system in a complete solar system model," *Celestial Mechanics and Dynamical Astronomy*, Vol. 115, 2013, doi:10.1007/s10569-012-9459-2.

[11] X. Hou and L. Liu, "On quasi-periodic motions around the triangular libration points of the real Earth–Moon system," *Celestial Mechanics and Dynamical Astronomy*, Vol. 108, 2010, doi:10.1007/s10569-010-9305-3.

[12] X. Hou and L. Liu, "On quasi-periodic motions around the collinear libration points in the real earth–moon system," *Celestial Mechanics and Dynamical Astronomy*, Vol. 110, 2011, doi:10.1007/s10569-011-9340-8.

[13] D. A. Dei Tos, "Automated Trajectory Refinement of Three-Body Orbits in the Real Solar System Model," M.S. Thesis, Politecnico di Milano, Italy, doi:10.13140/RG.2.2.11084.82561.

[14] B. Park and K. Howell, "Characterizing Transition-Challenging Regions Leveraging the Elliptic Restricted Three-Body Problem: L2 Halo Orbits," *AIAA SCITECH 2024 Forum*, doi:10.2514/6.2024-1455.

[15] K. Oguri, K. Oshima, S. Campagnola, K. Kakihara, N. Ozaki, N. Baresi, Y. Kawakatsu, and R. Funase, "EQUULEUS trajectory design," *The Journal of the Astronautical Sciences*, Vol. 67, No. 3, 2020, doi:10.1007/s40295-019-00206-y.

[16] K. Boudad, K. C. Howell, and D. C. Davis, "Analogs for Earth-Moon Halo Orbits and their Evolving Characteristics in Higher-Fidelity Force Models," *AIAA SCITECH 2022 Forum*, 2022, doi:10.2514/6.2022-1276.

[17] D. A. Dei Tos and F. Topputo, "On the advantages of exploiting the hierarchical structure of astrodynamical models," *Acta Astronautica*, Vol. 136, 2017, doi:10.1016/j.actaastro.2017.02.025.

[18] N. Baresi, "Transition of Two-Dimensional Quasi-periodic Invariant Tori in the Real-Ephemeris Model of the Earth–Moon System," *Modeling and Optimization in Space Engineering: New Concepts and Approaches*, pp. 33–59, Springer, doi:10.1007/978-3-031-24812-2_2.

[19] G. Gomez, A. Jorba, J. J. Masdemont, and C. Simo, *Dynamics and Mission Design Near Libration Points, Vol IV: Advanced Methods for Triangular Points*, Vol. 5. World Scientific, doi:10.1142/4336.

[20] R. S. Park, W. M. Folkner, J. G. Williams, and D. H. Boggs, "The JPL planetary and lunar ephemerides DE440 and DE441," *The Astronomical Journal*, Vol. 161, No. 3, 2021, doi:10.3847/1538-3881/abd414.

[21] B. Park and K. C. Howell, "Leveraging the elliptic restricted three-body problem for characterization of multi-year Earth-Moon L_2 halos in an ephemeris model," *AAS/AIAA Astrodynamics Specialist Conference, Big Sky, Montana, August 13-17, 2023.*,

[22] D. J. Scheeres, "The Restricted Hill Four-Body Problem with Applications to the Earth-Moon-Sun system," *Celestial Mechanics and Dynamical Astronomy*, Vol. 70, 1998, doi:10.1023/A:1026498608950.

[23] V. Szebehely, *Theory of Orbit: The Restricted Problem of Three Bodies*. Academic Press, doi:10.1016/B978-0-12-395732-0.X5001-6.

[24] S. T. Scheuerle Jr, K. C. Howell, and D. C. Davis, "Energy-informed pathways: A fundamental approach to designing ballistic lunar transfers," *Advances in Space Research*, doi:10.1016/j.asr.2024.07.035.

[25] M. Andreu, *The Quasi-bicircular Problem*. PhD Dissertation, Universitat de Barcelona, Spain,

[26] G. Gómez and J. Mondelo, "The dynamics around the collinear equilibrium points of the RTBP," *Physica D: Nonlinear Phenomena*, Vol. 157, No. 4, 2001, doi:10.1016/S0167-2789(01)00312-8.

[27] À. Jorba and J. Villanueva, "On the persistence of lower dimensional invariant tori under quasi-periodic perturbations," *Journal of Nonlinear Science*, Vol. 7, No. 5, 1997, doi:10.1007/s003329900036.

[28] Z. P. Olikara and D. J. Scheeres, "Numerical method for computing quasi-periodic orbits and their stability in the restricted three-body problem," *Advances in the Astronautical Sciences*, Vol. 145, No. 911-930, 2012,

[29] B. P. McCarthy and K. C. Howell, "Four-body cislunar quasi-periodic orbits and their application to ballistic lunar transfer design," *Advances in Space Research*, Vol. 71, No. 1, 2023, doi:10.1016/j.asr.2022.09.020.

[30] J. J. Rosales, À. Jorba, and M. Jorba-Cuscó, "Invariant manifolds near L_1 and L_2 in the quasi-bicircular problem," *Celestial Mechanics and Dynamical Astronomy*, Vol. 135, No. 15, doi:10.1007/s10569-023-10129-4.

[31] G. Gómez, J.-M. Mondelo, and C. Simó, "A collocation method for the numerical Fourier analysis of quasi-periodic functions. I. Numerical tests and examples," *Discrete and Continuous Dynamical Systems - B*, Vol. 14, No. 1, 2010, doi:10.3934/dcdsb.2010.14.41.

[32] M. Jorba-Cuscó, A. Farrés, and À. Jorba, "Two periodic models for the Earth-Moon system," *Frontiers in Applied Mathematics and Statistics*, Vol. 4, 2018, doi:10.3389/fams.2018.00032.

[33] L. T. Peterson, G. Brown, À. Jorba, and D. Scheeres, "Dynamics around the Earth–Moon triangular points in the Hill restricted 4-body problem," *Celestial Mechanics and Dynamical Astronomy*, Vol. 136, No. 4, 2024,